

Numerical Simulation of Three-Dimensional Heat Transfer and Plastic Flow During Friction Stir Welding

R. NANDAN, G.G. ROY, and T. DEBROY

Three-dimensional visco-plastic flow of metals and the temperature fields in friction stir welding have been modeled based on the previous work on thermomechanical processing of metals. The equations of conservation of mass, momentum, and energy were solved in three dimensions using spatially variable thermophysical properties and non-Newtonian viscosity. The framework for the numerical solution of fluid flow and heat transfer was adapted from decades of previous work in fusion welding. Non-Newtonian viscosity for the metal flow was calculated considering strain rate, temperature, and temperature-dependent material properties. The computed profiles of strain rate and viscosity were examined in light of the existing literature on thermomechanical processing. The heat and mass flow during welding was found to be strongly three-dimensional. Significant asymmetry of heat and mass flow, which increased with welding speed and rotational speed, was observed. Convective transport of heat was an important mechanism of heat transfer near the tool surface. The numerically simulated temperature fields, cooling rates, and the geometry of the thermomechanically affected zone agreed well with independently determined experimental values.

I. INTRODUCTION

FRICITION stir welding (FSW) is a solid-state welding process in which the welding is completed without melting of the base metal. A schematic diagram of the FSW system is presented in Figure 1. A rotating tool moves along the joint interface and generates heat. Movement of the solid and its deformation of a superplastic nature close to the tool forms the joint. The tool usually has a large-diameter shoulder and a smaller threaded pin.

Since its development in 1991 at TWI,^[1] FSW has been widely analyzed, both experimentally and using mathematical models.^[2–15] However, most of these models have focused on heat transfer calculations and disregarded plastic flow near the tool. Several earlier attempts to model FSW were based on analytical solution of the heat conduction equation for a thin plate. For example, Russel and Shercliff^[2] adapted analytical solutions of heat conduction equations to model FSW considering several simplified heat sources such as a point source, line source, and a distributed surface heat source. Gould and Feng^[3] also used the Rosenthal's analytical conduction model to predict a quasi-steady temperature field due to a moving point heat source at a constant velocity. They considered heat generation only at the tool shoulder. Schmidt *et al.*^[4] proposed a more general analytical model for heat generation based on various contact conditions at the tool/matrix interface, namely sliding, sticking, and partial sticking condition. They concluded that the sticking condition prevailed at the tool/matrix interface of AA 2024-T3 alloy, based on experimental data on heat generation rate and plunge force.

Several investigators used numerical heat transfer to understand the FSW process. However, the plastic flow was ignored in some of the initial studies. For example,

Frigaard *et al.*^[5] developed a numerical three-dimensional (3-D) heat flow model for FSW based on the finite difference method. They assumed that heat was generated at the tool shoulder due to frictional heating and adjusted the coefficient of friction so that the calculated peak temperature did not exceed the melting temperature. Chao *et al.*^[6] formulated heat transfer in the FSW process based on overall heat balance and inverse modeling into two boundary value problems (BVP)—a steady BVP for the tool and a transient BVP for the workpiece—and solved them using the finite element method (FEM). They found that only 5 pct of the heat generated was transported into the tool and about 80 pct of the mechanical work was dissipated as heat. Song and Kovacevic^[7,8] presented a detailed 3D numerical model of FSW where heat input from the tool was modeled as a moving heat source. Heat transfer during tool penetration and pulling was modeled. Later, Song and Kovacevic^[9] developed a transient 3D thermal model both for the tool and the workpiece. They achieved good agreement between the experimentally determined and computed temperatures. Khandkar *et al.*^[10] developed a 3D thermal model where the heat generation was modeled based on experimentally measured torque distribution. However, they adjusted the bottom heat transfer coefficient to achieve good agreement between the computed and the measured temperatures.

Most of the previous efforts to model thermal profiles in FSW did not consider 3D plastic flow. There are a few exceptions. Smith *et al.*^[13] experimentally determined viscosity as a function of shear rate and temperature for AA 6061-T6 alloy. The measured viscosity values were then incorporated into a 3D FSW model. They found that the viscous heat dissipation within the weld was the source of heat generation. Frictional heating did not significantly contribute to the heat generation. Ulysse^[14] used a 3D viscoplastic model to obtain a temperature profile in AA 7050-T7451 joints produced by FSW. However, the predicted temperatures were consistently higher than the corresponding experimental values. The discrepancy was attributed to inadequate representation of the constitutive behavior of the metal for a wide range of strain rates and temperatures typical of FSW.

R. NANDAN, Graduate Student, G.G. ROY, Visiting Scientist, and T. DEBROY, Professor, are with the Department of Materials Science and Engineering, The Pennsylvania State University, University Park, PA 16802, U.S.A. Contact e-mail: debroy@psu.edu

Manuscript submitted August 29, 2005.

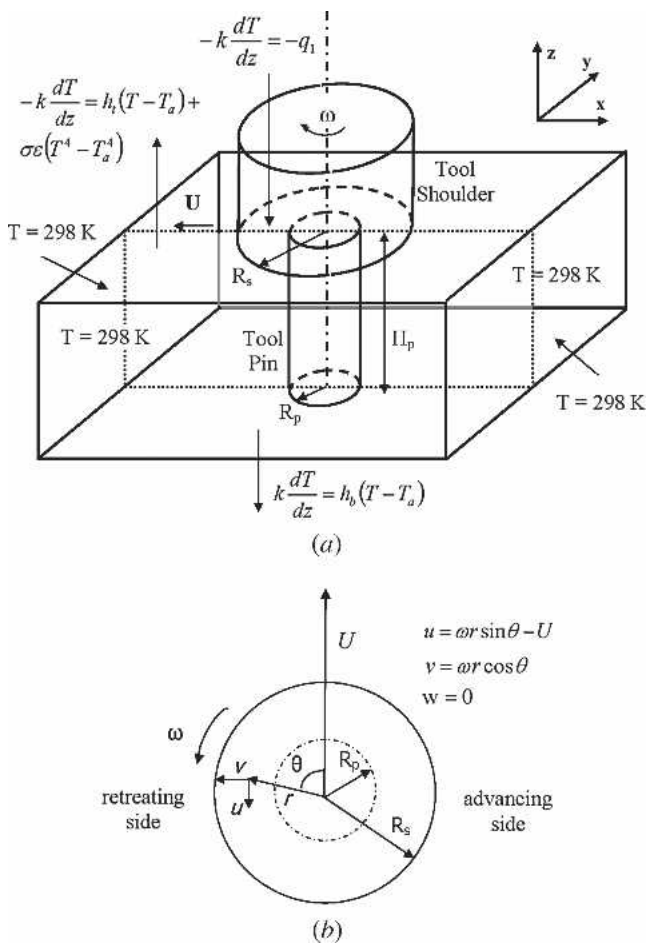


Fig. 1—(a) Schematic diagram of the FSW system considered in the model showing the thermal boundary conditions. (b) Top view of the tool showing velocity boundary conditions at the tool surface.

Recently, Colegrove and Shercliff^[15] developed a 3D model of heat and mass transfer using a commercial computer code, FLUENT, to understand the temperature distribution and material flow around a complex threaded tool. No slip condition was assumed at the tool/workpiece interface. The model overpredicted the size of the deformation zone, and the effect of the rotational speed on peak temperature could not be adequately represented by the model. They suggested that these problems could be addressed in the future either by using a material slip at the tool interface or dramatically reducing the viscosity near the solidus temperature in the FLUENT code.

The previous work represents significant progress in the quantitative understanding of the FSW process. However, several important questions remain unanswered. For example, can the viscoplastic flow of metals be reliably predicted based on the previous work in extrusion and thermomechanical processing of metals? Can our current understanding of thermomechanical processing adequately represent the spatial variation of viscosity and strain rate in the workpiece during FSW? What would be the typical cutoff viscosity beyond which significant material flow does not occur? Can the numerical solution framework typically used in the heat transfer and fluid flow calculations in fusion welding be used in the FSW process? Can

the cooling rates and the shape of the thermomechanically affected zone be reliably predicted?

Here we show that the temperature fields, cooling rates, the plastic flow fields, and the geometry of the thermomechanically affected zone (TMAZ) can be adequately described by solving the equations of conservation of mass, momentum, and energy in three dimensions with appropriate boundary conditions. The model considers tool design-dependent spatially variable heat-generation rates that account for the deformation work, non-Newtonian viscosity as a function of local strain rate, temperature, and the nature of the material, and temperature-dependent thermal conductivity and specific heat and yield stress. Numerically computed temperature fields, variations of peak temperatures with FSW variables, and TMAZ geometry were compared with the corresponding independently measured values reported in the literature.

II. MATHEMATICAL MODELING

A. Assumptions

Except at the beginning and end of welding, heat is generated at a constant rate during most of the intermediate period, and the cross-sections of the welds demonstrate similar geometry, structure, and properties, indicating a quasi-steady behavior. Shortly after the start of welding, the cylindrical tool shoulder and the tool pin rotate at a constant rotational speed with the tool pin completely inserted within the workpiece. The mass flow is treated as a flow of a non-Newtonian, incompressible, viscoplastic material. The maximum shear stress for yielding was assumed to be:

$$\tau = \sigma_{yield} / \sqrt{3}$$

where the yield stress σ_{yield} is based on distortion energy theory for plane stress. The density variation was ignored following Boussinesq's approximation. Partial sticking condition at the tool shoulder interface and full sticking conditions at the tool pin interfaces were considered. The extent of slip between the shoulder and the workpiece was adjusted to achieve good agreement between the computed and the measured^[9] temperatures.

B. Governing Equations

The continuity equation for incompressible single-phase flow in index notation for $i = 1, 2,$ and $3,$ representing $x, y,$ and z directions respectively, is given by:

$$\frac{\partial u_i}{\partial x_i} = 0 \quad [1]$$

where $u =$ the velocity of plastic flow. The steady single-phase momentum conservation equations with reference to a coordinate system attached to the heat source in index form may be represented as:^[16]

$$\rho \frac{\partial u_i u_j}{\partial x_i} = -\frac{\partial P}{\partial x_j} + \frac{\partial}{\partial x_i} \left(\mu \frac{\partial u_j}{\partial x_i} + \mu \frac{\partial u_i}{\partial x_j} \right) - \rho U \frac{\partial u_j}{\partial x_j} \quad [2]$$

where ρ = the density, μ = the non-Newtonian viscosity, U = the welding velocity, and P = the pressure. The calculation of viscosity requires local values of strain rate and temperature. The viscosity was calculated based on the following formulation of flow stress, σ_e , proposed by Sheppard and Wright:^[17]

$$\sigma_e = \frac{1}{\alpha} \sinh^{-1} \left[\left(\frac{Z}{A} \right)^{1/n} \right] \quad [3]$$

where A , α , and n = material constants and Z = the Zener-Hollomon parameter that represents the temperature-compensated effective strain rate and is given by:

$$Z = \dot{\epsilon} \exp\left(\frac{Q}{RT}\right) \quad [4]$$

Here Q = the temperature-independent activation energy, R = gas constant, and $\dot{\epsilon}$ is the effective strain rate and is given by

$$\dot{\epsilon} = \left(\frac{2}{3} \epsilon_{ij} \epsilon_{ij} \right)^{1/2} \quad [5]$$

where ϵ_{ij} is the strain rate tensor, defined as

$$\epsilon_{ij} = \frac{1}{2} \left(\frac{\partial u_i}{\partial x_j} + \frac{\partial u_j}{\partial x_i} \right) \quad [6]$$

An expanded form of Eq. [6], needed for the strain rate calculation, is given in Appendix A. Finally, viscosity can be determined from flow stress and effective strain rate from:^[18]

$$\mu = \frac{\sigma_e}{3\dot{\epsilon}} \quad [7]$$

The above formulation indicates that viscosity is a strong function of local strain rate and temperature. The material constants needed for the calculation of viscosity were experimentally determined by Sheppard and Jackson.^[19] Figure 2 shows the computed variation of viscosity, expressed as logarithm to the base of 10, with strain rate and temperature. The results show that viscosity decreases significantly with both strain rate and temperature. The strain rate is the more dominant factor for the conditions typical of FSW.

The steady thermal energy conservation equation is given by:

$$\rho C_p \frac{\partial(u_i T)}{\partial x_i} = -\rho C_p U \frac{\partial T}{\partial x_i} + \frac{\partial}{\partial x_i} \left(k \frac{\partial T}{\partial x_i} \right) + [S(\theta) A_r / V] \quad [8]$$

where ρ = the density, C_p = the specific heat, k = the thermal conductivity of the weld material, $S(\theta)$ = the heat generation rate per unit area at the tool pin and workpiece interface, A_r = any arbitrarily selected area on the tool pin, and V = the volume over which the heat generated on A_r is

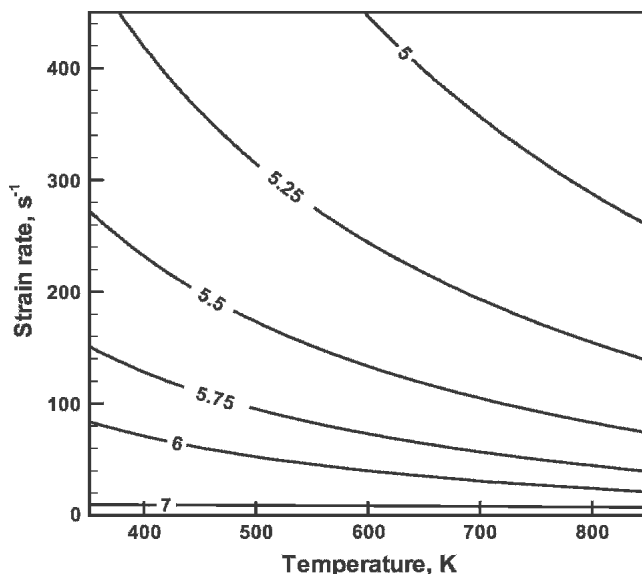


Fig. 2—Computed contours of viscosity as a function of temperature and strain rate. The viscosity in kg/m-s is expressed as logarithm to the base 10.

dissipated. The heat source $S(\theta)$ for the vertical surface of the tool pin may be defined as:

$$S(\theta) = C_f \tau (\omega R_p - U \sin \theta) \quad [9a]$$

Similarly, $S(\theta)$ for the horizontal bottom surface of the tool pin is given by:

$$S(\theta) = C_f \tau (\omega r - U \sin \theta) \quad [9b]$$

where C_f = the power efficiency factor (*i.e.*, the amount of mechanical energy converted to heat energy), the angular velocity ω is given by $2\pi N$, where N is the number of revolutions per second, and R_p is the tool pin radius. The velocity $(\omega r - U \sin \theta)$ represents the relative velocity of the tool with respect to the material. The variation of yield stress for AA 6061-T6 alloy with temperature is shown in Figure 3 based on data available in Reference 20. The symbol θ represents the angle between a horizontal-direction vector from the tool axis to any point on the cylindrical surface and the welding direction and may be defined in the Cartesian coordinate system as:

$$\theta = \sin^{-1} \left(\frac{y}{\sqrt{x^2 + y^2}} \right), \text{ or } \theta = \cos^{-1} \left(\frac{x}{\sqrt{x^2 + y^2}} \right) \quad [10]$$

where (0,0) corresponds to the tool axis. Since the thermal conductivity of the workpiece is about eight times higher than of the steel tool material, most of the heat generated at the tool shoulder/workpiece interface will be transported into the workpiece. Therefore, the heat generated at the tool shoulder can be prescribed as a flux at the top surface of the workpiece.

Since the yield strength data were obtained for very low strain rates, it is important to examine the validity of these

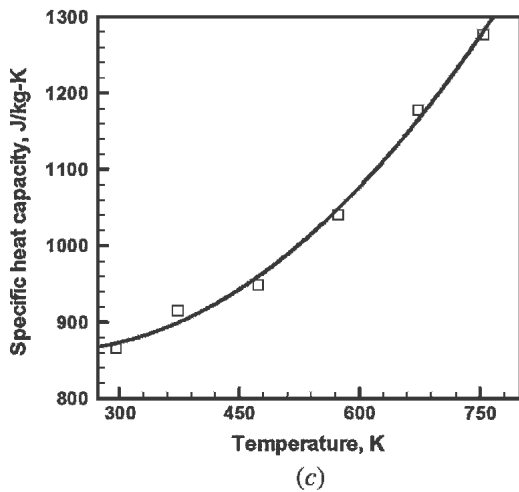
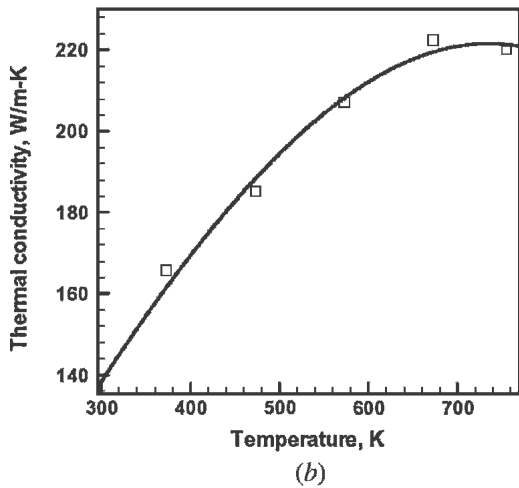
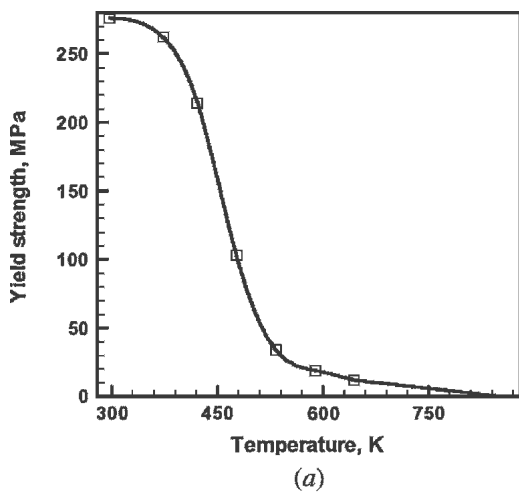


Fig. 3—Variations of (a) yield strength,^[20] (b) thermal conductivity,^[14] and (c) specific heat capacity^[14] of AA 6061-T6 alloy with temperature. Symbols denote data points from the literature; the curves are obtained by spline interpolation of the data points.

data for strain rates encountered typically in FSW. Experimental data on the variation of yield strength as a function of strain rate for 6061-T6 aluminum alloy indicate that the yield strength increases significantly only when the strain

rate exceeds 1000 seconds⁻¹. The high critical strain rate represents a shift in the mechanism of deformation from cutting or bypassing of discrete obstacles by moving dislocations at low strain rates to phonon or electron drag on moving dislocations at high strain rates.^[21] Since the strain rates encountered in FSW are much lower than 1000 seconds⁻¹, the yield strength was assumed to be independent of strain rate.

C. Boundary Conditions

The main boundary conditions for temperature are shown in Figure 1(a), while the boundary conditions for velocities at the top surface are shown in Figure 1(b). The details of boundary conditions are discussed here. A heat flux continuity at the shoulder matrix interface yields:

$$k \left. \frac{\partial T}{\partial z} \right|_{\text{top}} = q_1 \quad \text{in the range } R_p \leq r \leq R_s \quad [11]$$

R_p and R_s = the tool pin and shoulder radius, respectively, and q_1 = the rate of heat generation due to plastic work at the shoulder/workpiece interface. It is given by:

$$\begin{aligned} q_1 &= C_f [\delta \tau (\omega r - U \sin \theta) + (1 - \delta) \mu P_T] \\ &= C_f \left[\delta \tau \left(\omega \sqrt{(x^2 + y^2)} - U \frac{y}{\sqrt{(x^2 + y^2)}} \right) \right. \\ &\quad \left. + (1 - \delta) \mu P_T \right] \end{aligned} \quad [12]$$

where δ = the extent of sticking and P_T = the applied pressure (plunge) on the shoulder. When $\delta = 1$, full sticking is indicated and all heat is generated by plastic deformation. When $\delta = 0$, heat is generated only by friction. The boundary condition for heat exchange between the top surface of the workpiece and the surroundings beyond the shoulder involved consideration of both convective and radiative heat transfer as

$$-k \left. \frac{\partial T}{\partial z} \right|_{\text{top}} = \sigma \varepsilon (T^4 - T_a^4) + h_t (T - T_a) \quad [13]$$

where σ = the Stefan-Boltzmann constant, ε = the emissivity, h_t = the heat transfer coefficient at the top surface, and T_a = the ambient temperature. At the bottom surface, Newtonian cooling under natural convection has been applied:

$$k \left. \frac{\partial T}{\partial z} \right|_{\text{bottom}} = h_b (T - T_a) \quad [14]$$

where h_b is the heat transfer coefficient at the bottom surface of the workpiece. Velocity at the tool pin periphery has been defined in terms of tool translation velocity and the tool pin angular velocity:

$$\begin{aligned} u &= \omega R_p \sin \theta - U \\ v &= \omega R_p \cos \theta \end{aligned} \quad [15]$$

Similarly, at the shoulder contact, velocity condition may be written as:

$$\left. \begin{aligned} u &= \omega r \sin \theta - U \\ v &= \omega r \cos \theta \end{aligned} \right\} \text{ in the range } R_p \leq r \leq R_s \quad [16]$$

At all other surfaces, temperatures are set at ambient temperature and the velocities are set to zero.

The governing equations and the boundary conditions were implemented in a computer code. The discretization of the governing equations, implementation of the boundary conditions, and the convergence and accuracy of the solutions are described in Appendix B. The SIMPLE algorithm^[22] based solution procedure, capable of calculating 3D heat transfer and fluid flow with a stationary or moving heat source, with a free or flat surface, has been well tested and has been recently reported for the calculations of heat transfer and fluid flow in several welding processes.^[16,23–28] The data used for the calculations are presented in Tables I and II.

III. RESULTS AND DISCUSSION

A. Heat Generation Rates

The proportion of the heat generated at the tool shoulder and the pin surfaces is determined by the tool geometry and the welding variables. For the experimental conditions studied in this work, the computed heat generation rates at the shoulder and the pin surfaces are presented in Table III. The results show that depending on the welding conditions, between 80 to 90 pct heat is generated at the tool shoulder and the remaining amount at other tool surfaces. Figure 4 shows the spatial variation of the heat generation pattern at the tool/workpiece interfaces. Figure 4(a) shows that the

heat generation pattern at the tool shoulder is nearly symmetric about the tool axis. More heat is generated further away from the axis owing to higher relative velocity between the workpiece and the shoulder. The heat generation rate at the bottom of the pin (Figure 4(b)) indicates a similar behavior. Here, the total amount of heat generated is considerably lower than that at the shoulder because of the smaller radius of the pin and the lower relative velocity between the pin and the workpiece. The angular variation of the heat generation rate on the tool surface is shown in Figure 4(c). The nonuniformity in the heat generation pattern results from the difference in the relative velocity at different angular locations on the pin surface, which arises due to the variation in term $U \sin \theta$. The local differences in the heat generation rates lead to angular variations of temperature on the tool surface. As a result, meaningful modeling of temperature and plastic flow fields must consider 3D heat transfer.

B. Computed Temperature Fields

The computed temperature profiles along the longitudinal and transverse sections through the tool axis and at the top surface of the workpiece are shown in Figures 5(a), (b), and (c), respectively. The temperature profiles on the longitudinal midsection (Figure 5(a)) and on the top surface of the workpiece (Figure 5(c)) are compressed in front of the tool and expanded behind it. The computed results are consistent with the fact that heat is supplied to the cold region of the workpiece ahead of the tool, while heat is transported to material already preheated behind the tool. This asymmetry results from the motion of the tool and becomes more prominent at high welding speeds. The temperature profile in Figure 5(b) is also somewhat asymmetric. It can be observed that the region near the tool pin is hotter toward the advancing side compared to the retreating side. This asymmetry originates from the local differences in the heat generation rates shown in Figure 4(c) due to local variations in the relative velocities between the tool surface and the workpiece.

Figure 6 depicts the computed thermal cycles at several monitoring locations. The locations are 2 mm below the top surface of the workpiece and at 8, 12, 16, and 25 mm from the welding direction in the retreating side. Thermal cycles were constructed from the steady-state temperature distribution by converting distance to time using welding velocity. The results show a rapid increase in temperature during heating followed by a comparatively slower cooling as the heat source moves away from the monitoring locations. This behavior may be further explained from the temperature contours similar to those in Figure 5(c). The initial steep heating is observed as the monitoring locations encounter compressed thermal contours ahead of the tool. As the tool moves ahead of the monitoring locations, the expanded temperature contours lead to slow cooling. The higher the welding velocity, the faster the temperature changes during both heating and cooling.

The computed temperature profiles at four monitoring locations are compared with independent experimental data from the literature^[9] in Figure 7. Good agreements between the experimentally determined and the computed results at

Table I. Data Used in the Calculations

| Property/Parameter | Value |
|---|--------------------------------------|
| Workpiece length (<i>x</i> -direction) | 0.254 m |
| Workpiece width (<i>y</i> -direction) | 0.102 m |
| Shoulder radius | 25 mm |
| Tool radius | 6 mm |
| Pin length | 12.7 mm |
| Tool speed | 0.4 to 1.8 mm/s |
| Rotational speed | 100 to 800 rpm |
| Workpiece-material | AA 6061 |
| Density | 2700 kg/m ³ |
| Solidus temperature ^[20] | 855 K |
| Plunge pressure, ^[9] P_T | 12.7 MPa |
| Coefficient of friction ^[9] | 0.4 |
| Percentage sticking, ^[9] δ | 0.65 |
| Coefficient of thermal expansion ^[20] | $2.36 \times 10^{-5} \text{ K}^{-1}$ |
| Heat transfer coefficient ^[6] | 30 W/m ² -K |
| A , ^[19] material constant in Eq. [3] | $8.86 \times 10^6 \text{ s}^{-1}$ |
| α , ^[19] material constant in Eq. [3] | 0.045 (MPa)^{-1} |
| n , ^[19] material constant in Eq. [3] | 3.55 |
| Q , ^[19] activation energy | 145 kJ/mol |
| Tool material | Tool Steel - H13 |
| Density | 7800 kg/m ³ |
| Thermal conductivity of solid ^[9] | 25 W/m-K |

Table II. Temperature-Dependent Thermophysical Property Values of AA 6061-T6 Alloy

| Property | Temperature Range (K) | C_0 | C_1 | C_2 | C_3 | Reference |
|--------------------------------|-----------------------|----------------------|-------------------------|-------------------------|-------------------------|-----------|
| Yield strength, MPa | 298 to 372 | 1.003×10^3 | -7.295×10^0 | 2.448×10^{-2} | -2.747×10^{-5} | 20 |
| | 373 to 421 | -3.277×10^3 | -2.558×10^1 | 7.351×10^{-2} | -7.129×10^{-5} | |
| | 421 to 476 | -1.528×10^4 | 1.064×10^2 | -2.392×10^{-1} | 1.757×10^{-4} | |
| | 477 to 532 | 5.228×10^3 | -2.264×10^1 | 3.129×10^{-2} | -1.331×10^{-5} | |
| | 533 to 588 | 1.280×10^4 | -6.525×10^1 | 1.112×10^{-1} | -6.330×10^{-5} | |
| | 589 to 643 | -9.106×10^2 | 4.575×10^0 | -7.320×10^{-3} | 3.789×10^{-6} | |
| Specific heat capacity, J/kg-K | 644 to 855 | 4.863×10^1 | -5.687×10^{-2} | 0 | 0 | 14 |
| | 298 to 855 | 9.293×10^2 | -6.270×10^{-1} | -1.481×10^{-3} | -4.330×10^{-8} | |
| Thermal conductivity, W/m-K | 298 to 855 | 2.522×10^1 | 3.978×10^{-1} | 7.358×10^{-6} | -2.518×10^{-7} | 14 |

Property values are given by $C_0 + C_1T + C_2T^2 + C_3T^3$, where T is any temperature in the given temperature range.

Table III. Heat Generated at Various Surfaces of the Tool

| Weld Speed (mm/s) | Rotational Speed (rpm) | Heat Input from Shoulder (kW) | Heat Input from Tool Pin (W) | Heat Input from Tool Bottom (W) | Maximum Temperature (K) |
|-------------------|------------------------|-------------------------------|------------------------------|---------------------------------|-------------------------|
| 0.5 | 200 | 2.97 | 250.1 | 45.6 | 700.2 |
| 1.0 | 200 | 3.05 | 252.8 | 46.1 | 694.4 |
| 1.5 | 200 | 3.17 | 258.5 | 47.7 | 688.2 |
| 0.5 | 400 | 3.72 | 213.9 | 61.9 | 762.7 |
| 1.0 | 400 | 3.72 | 215.5 | 62.1 | 756.0 |
| 1.5 | 400 | 3.88 | 216.2 | 63.4 | 749.6 |
| 0.5 | 600 | 4.23 | 164.3 | 76.2 | 807.4 |
| 1.0 | 600 | 4.31 | 168.1 | 77.0 | 801.5 |
| 1.5 | 600 | 4.47 | 172.3 | 77.4 | 797.3 |

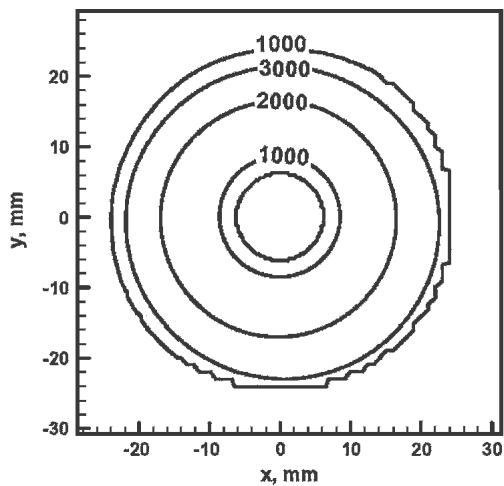
different monitoring locations indicate that the model can be used to examine the temperature profiles and cooling rates. It may be noted here that the peak temperatures in four locations are in the range of about 780 to 800 K. The relatively small differences in the peak temperatures in these locations result from two factors. First, all the locations lie within the TMAZ, where rapid heat transfer occurs due to convective flow. Second, the high thermal conductivity of the aluminum alloy also contributes to thermal homogeneity. Figure 8(a) shows the variation of peak temperature with welding velocity at different power efficiency factors. The figure indicates that the peak temperature decreases with increase in welding velocity. This behavior originates from the fact that at higher welding velocity, the heat input per unit length decreases and heat is dissipated over a wider region of the workpiece. It is also observed that peak temperature becomes higher with higher power efficiency factors, as expected. Figure 8(b) shows that peak temperature increases with increase in rotational velocity and power efficiency factor. At high rotational speed, the relative velocity between the tool and workpiece is high, and consequently the heat generation rate and the temperatures are also high.

C. Computed Viscosity and Plastic Flow Fields

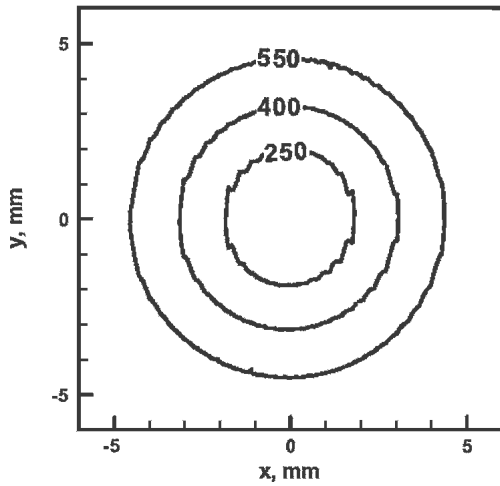
Figure 9 shows the computed strain rate *versus* distance along the x -direction at different elevations (*i.e.*, values of z). For low values of z , maximum strain rate occurs at the

surface of the pin where the velocity gradient is highest. At high values of z (*i.e.*, near the top surface of the workpiece), the velocity gradient is highest near the outer edge of the tool shoulder. As a consequence, at $z = 11.47$ -mm plane, the computed strain rate is highest at $x = 25$ mm. It may be observed that the order of magnitude of strain rate is higher than 100/seconds near the shoulder, which sharply drops to about 30/seconds at about 4 mm below the shoulder. Frigaard *et al.*^[5] measured grain size, estimated peak temperature from a thermal model, and estimated maximum strain rate to be of the order of 20/seconds. Computed values of strain rates are somewhat higher than expected. The strain rates decrease rapidly with depth due to a large decrease in velocities through viscous dissipation.

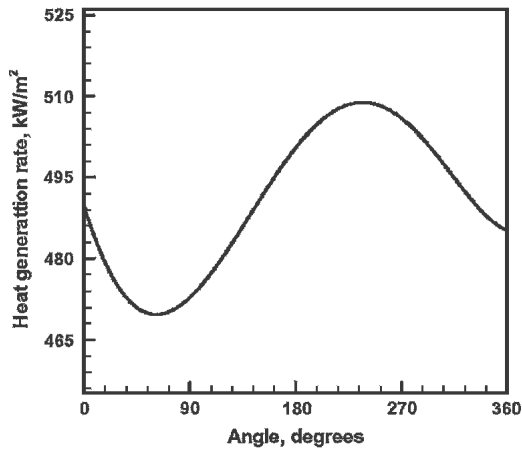
Figure 10 shows the variation of viscosity along the x -direction at different elevations (*i.e.*, values of z). It is seen that at $z = 11.47$ mm (*i.e.*, 0.8 mm below the top surface), viscosity decreases with increase in x close to the tool bit, followed by a sharp increase at high values of x . Since the viscosity is inversely proportional to the local strain rate, this observation may be explained considering the values of strain rates presented in Figure 9, where the strain rate trends are just opposite to those of the viscosity values presented in Figure 10. At lower values of z , the viscosity progressively increases with x -distance, which is also consistent with the strain rate variations shown in Figure 9. An important consequence of the computed viscosity profiles is that high viscosity values beyond a certain critical high value result in lack of plastic flow



(a)

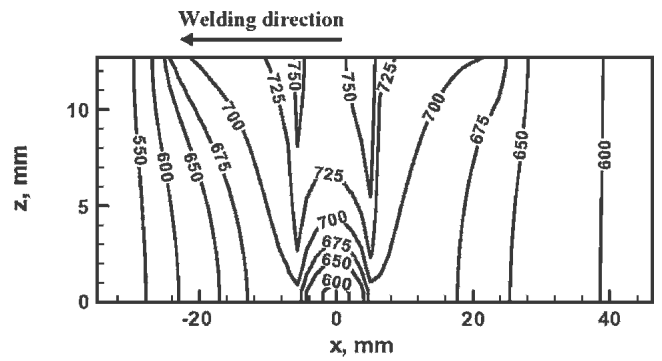


(b)

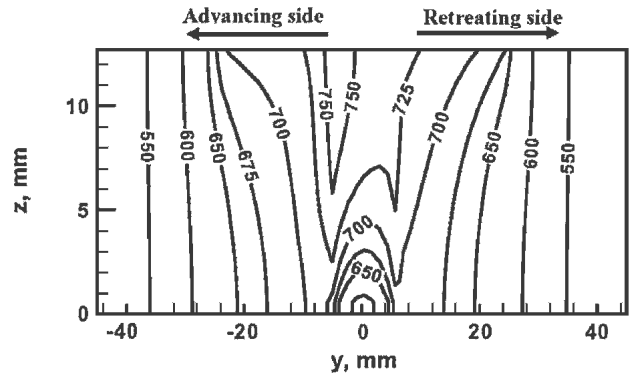


(c)

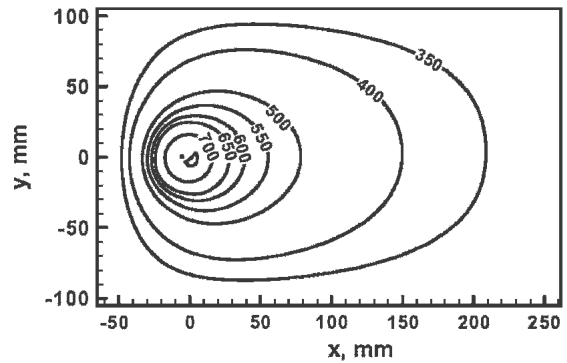
Fig. 4—Spatially variable heat generation rate at (a) tool shoulder, (b) bottom of tool pin, and (contour values are in kW/m^2) (c) curved surface of tool pin (values lie on a horizontal circle 1.27 mm below the top surface). The welding velocity was 1.59 mm/s and the tool rotational speed was 344 rpm.



(a)



(b)



(c)

Fig. 5—Computed temperature profiles (K) in (a) $y = 0$ (XZ plane), (b) $x = 0$ (YZ plane), and (c) $z = 12.7$ mm (XY plane) (*i.e.*, the top surface of the workpiece). The welding velocity was 1.59 mm/s and the tool rotational speed was 344 rpm.

and define the geometry of the TMAZ, as will be discussed subsequently.

Figure 11 shows the variation of u -component of velocity at different elevations (*i.e.*, z values). It is observed that at $z = 11.47$ mm, u -velocity increases and attains a maximum at around $x = 20$ mm, followed by a rapid decrease, while at planes near the bottom of the workpiece, the velocity peaks are attained at the tool surface. The velocity peaks increase and shift further away from the tool surface at higher elevations or z values because of the effect of shoulder. Near the top surface, the effect of shoulder and the viscous momentum transfer is fairly pronounced, resulting in high

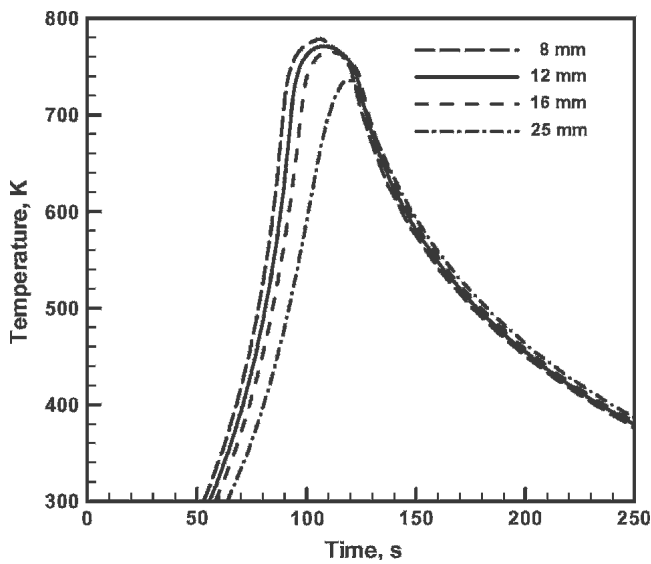


Fig. 6—Time/temperature profiles at several monitoring locations 2 mm below the top surface and at 8, 12, 16, and 25 mm from the centerline perpendicular to the welding direction in the retreating side. The welding velocity was 1.59 mm/s and the tool rotational speed was 344 rpm.

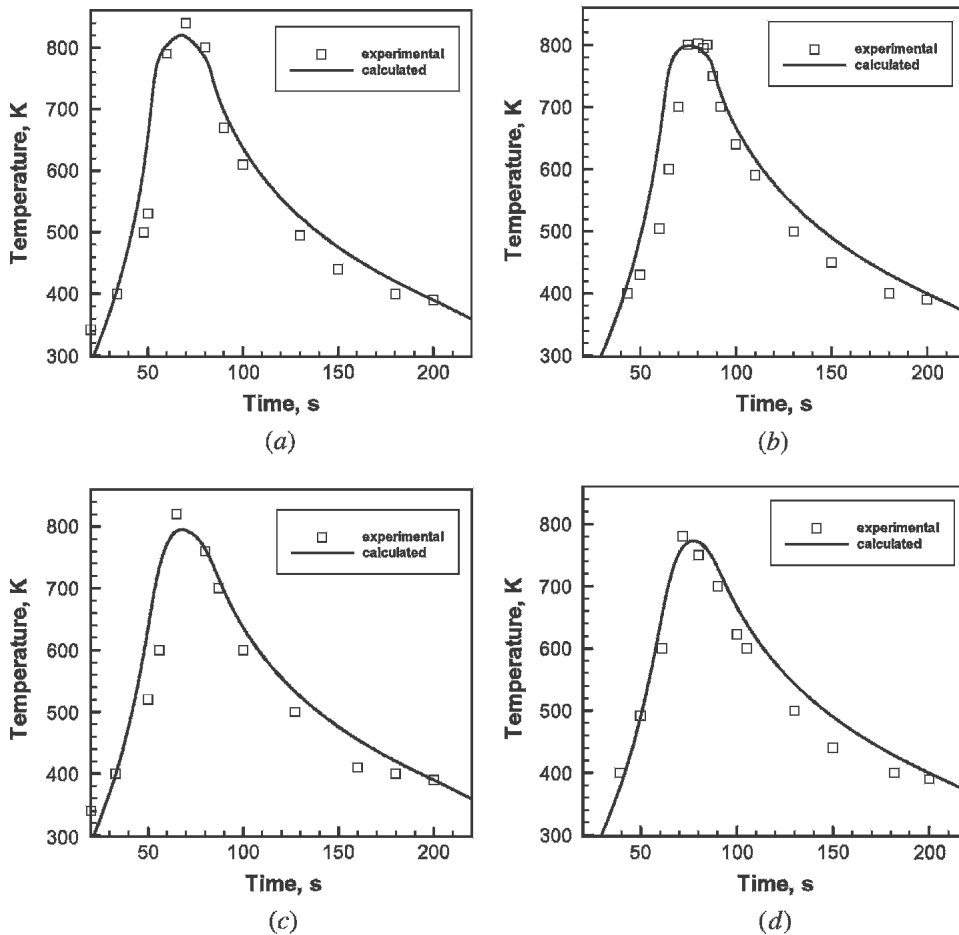
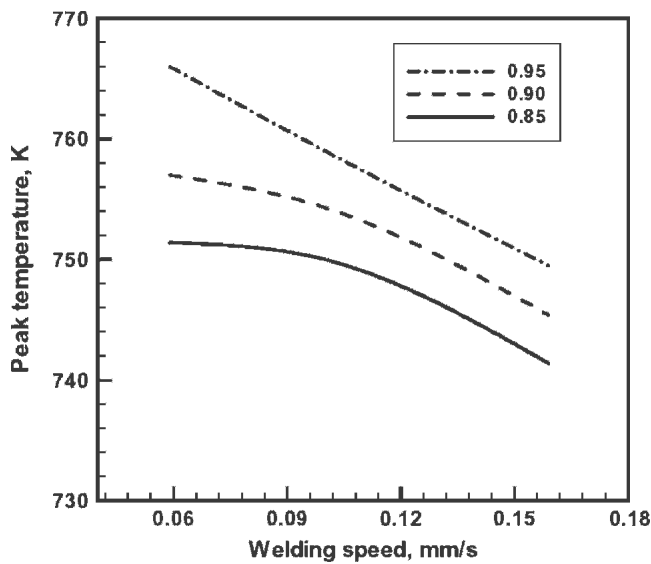


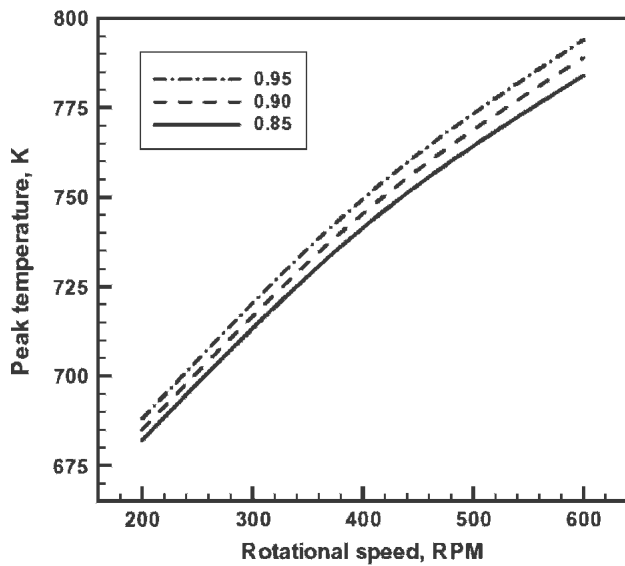
Fig. 7—Comparison between experimental^[9] and calculated time/temperature profile at points (a) 2 mm below the top surface and 8 mm from the centerline, (b) 2 mm below the top surface and 16 mm from the centerline, (c) 8 mm below the top surface and 8 mm from the centerline, and (d) 8 mm below the top surface and 16 mm from the centerline. The points are located in advancing side and the distances are perpendicular to the weld center line. The welding velocity was 1.59 mm/s and the rotational speed was 637 rpm.

peak velocity. But since momentum decays rapidly in the z -direction away from the shoulder, the effect of rapid rotation of the shoulder does not reach the lower elevations near the bottom of the workpiece. The high velocity near the top surface of the workpiece is achieved because of the tool shoulder velocity, but the velocities decay progressively downward from the top surface of the workpiece. Figure 11 shows that the velocity drops below 10 mm/s beyond the shoulder periphery. The momentum transfer in the vertical direction occurs entirely by viscous transport, and the effect of shoulder is most pronounced in planes at mid-thickness or above, where the order of magnitude of velocities is about 30 mm/s at about 1 mm from the tool pin surface. The velocity drops gradually thereafter to 10 mm/s and lower away from the tool pin.

The viscosity contours at different horizontal planes (*i.e.*, z values) are shown in Figure 12. The velocity vectors are also plotted in this figure, superimposed on the viscosity contours. It is readily observed that the order of magnitude of viscosity lies in the range of 10^5 to 5×10^6 Pa-s. This range is consistent with the values of non-Newtonian viscosity usually observed in typical viscoplastic processing of materials such as extrusion.^[29] At the top surface, the



(a)



(b)

Fig. 8—Peak temperature as a function of (a) welding velocity, with 400 rpm rotational speed and efficiency of heating = 0.85, 0.90, and 0.95 and (b) rotational speed, with 1.59 mm/s welding velocity and efficiency of heating = 0.85, 0.90, and 0.95.

minimum value of viscosity is attained at the shoulder tip, where the tool velocity, temperature, and strain rates are also highest in the entire domain. The viscosity decreases gradually from the tool tip radially outward. Figure 12 shows that viscosity increases significantly along the same direction away from the tool. No significant flow occurs when the viscosity is very high. The region of plastic flow decreases with depth.

Figure 13 depicts the temperature contours and velocity vectors on different horizontal planes. An interesting feature to note here is that the area that contains the high temperature contours and plastic flow decreases with distance from the workpiece top surface. The effect of the tool shoulder as a source of heat and momentum is most pro-

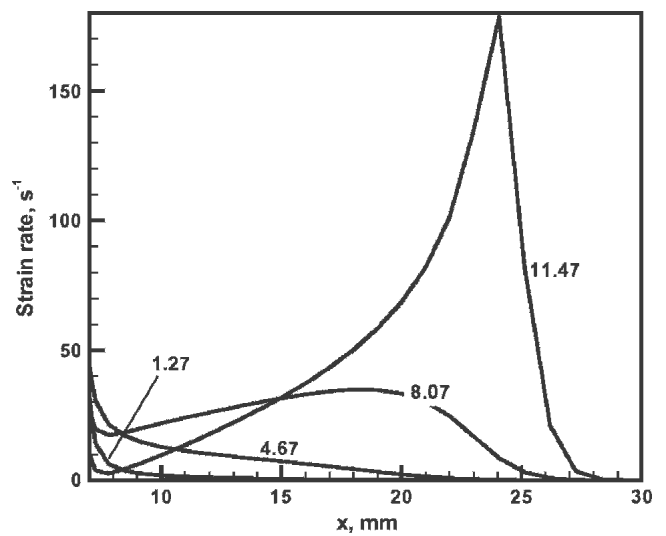


Fig. 9—Spatial variation of strain rate at different horizontal planes at $z = 1.27, 4.67, 8.07,$ and 11.47 mm. The welding velocity was 1.59 mm/s and the rotational speed was 344 rpm.

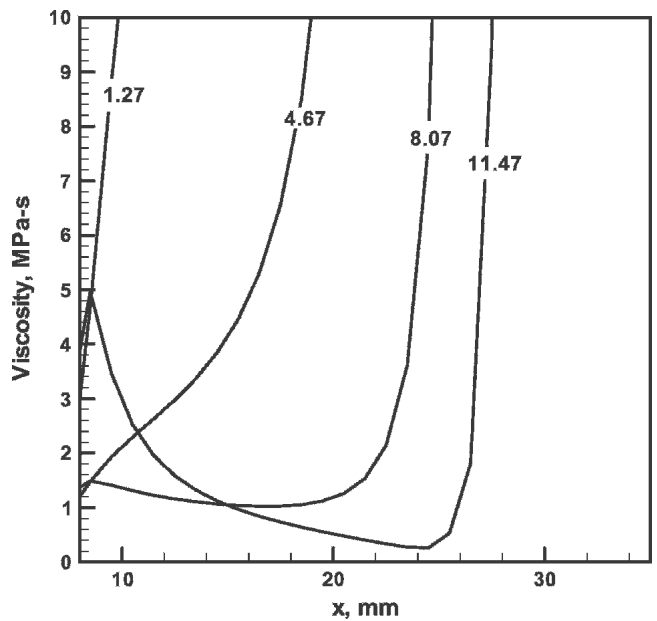


Fig. 10—Plot of variation of viscosity as a function of distance from tool surface at planes corresponding to $z = 1.27, 4.67, 8.07,$ and 11.47 mm. The welding velocity was 1.59 mm/s and the rotational speed was 344 rpm.

nounced in the upper half of the workpiece. The reduction in the area where the flow occurs with distance from the shoulder produces the characteristic shape of the TMAZ.^[5,9] Figure 14(a) depicts the shape of the TMAZ as obtained by drawing the isoviscosity surface for the critical viscosity, 5×10^6 Pa-s, above which no significant plastic flow occurs. Figure 14(b) compares the predicted TMAZ profile with that reported in an independent investigation.^[9] The predicted TMAZ geometry agrees well with the experimental result.

The relative rates of heat transfer by convection and conduction are determined by the Peclet number, Pe:

$$Pe = \frac{\rho u C_p L_R}{k} \quad [17]$$

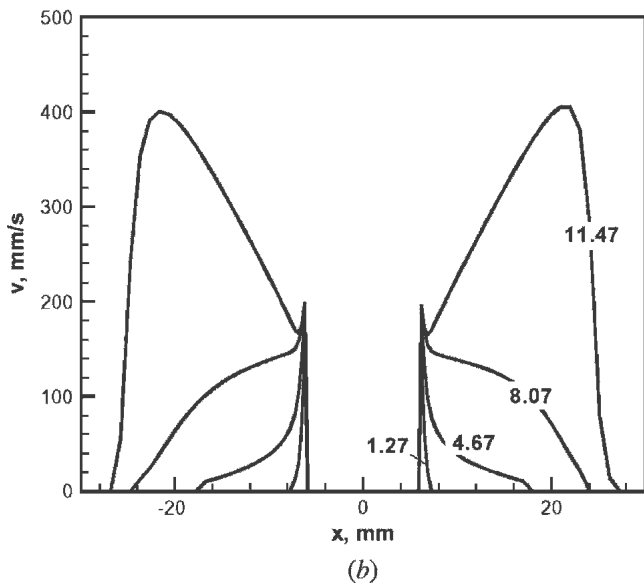
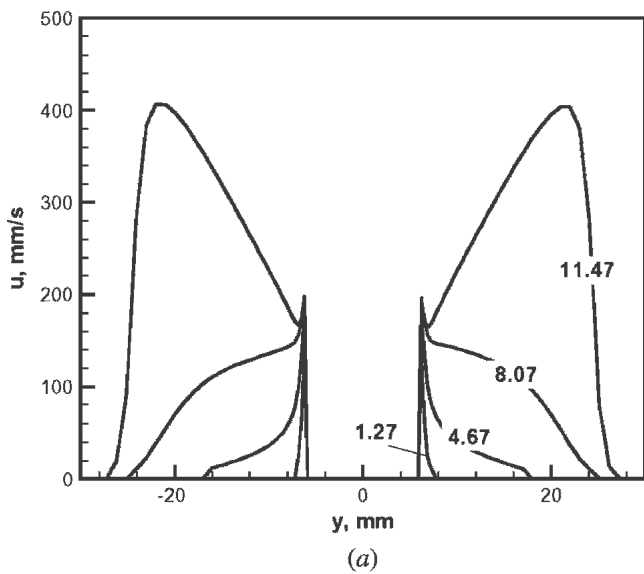


Fig. 11—Plot of variation of (a) u -velocity and (b) v -velocity as a function of distance from tool surface corresponding to $z = 11.47, 8.07, 4.67,$ and 1.27 mm for a 12.7-mm-thick plate. The welding velocity was 1.59 mm/s and the rotational speed was 344 rpm.

where u = the velocity, ρ = the density, C_p = the specific heat, L_R = the characteristic length taken as boundary layer thickness at the tool-workpiece interface, and k = the thermal conductivity. Considering a horizontal plane 3.7 mm below the top surface of the workpiece, the maximum velocity is about 300 mm/s at the surface of the pin and the length over which momentum diffusion occurs is about 6.67 mm. Taking 150 mm/s as the characteristic velocity and 3.33 mm as the characteristic length, the value of the Peclet number is 5.7. Although the aluminum alloy has a high thermal conductivity, the computed value of the Peclet number indicates that forced convection is still very important for heat transfer. However, in regions far away from the tool where no plastic flow occurs, heat transfer occurs by conduction.

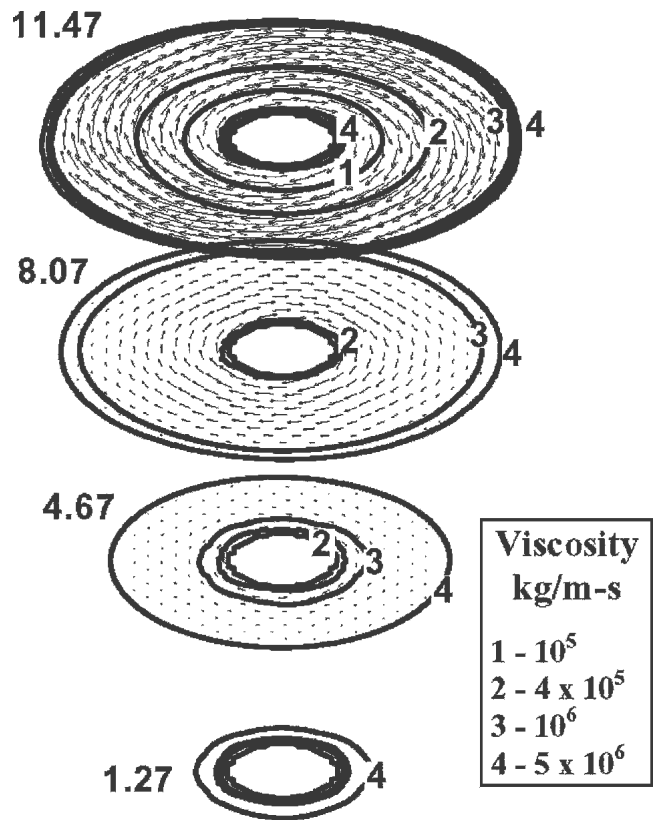


Fig. 12—Plot of spatial variation of viscosity at planes corresponding to $z = 1.27, 4.67, 8.07,$ and 11.47 mm. Distances in the x and y direction are equivalent, but the distance in the z direction is increased eightfold to enhance clarity. The welding velocity was 1.59 mm/s and the rotational speed was 637 rpm.

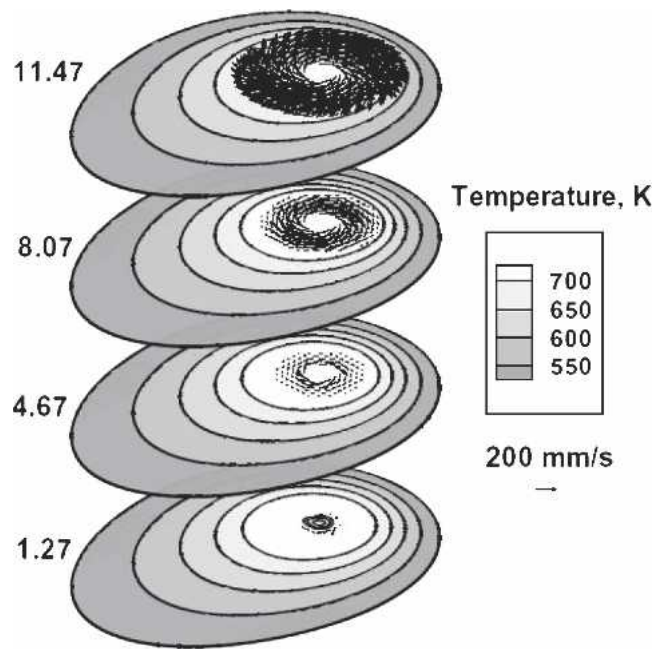


Fig. 13—Plot of temperature and velocity fields at the top surface and at planes $z = 1.27, 4.67, 8.07,$ and 11.47 mm. The welding velocity was 1.59 mm/s and the rotational speed was 637 rpm.

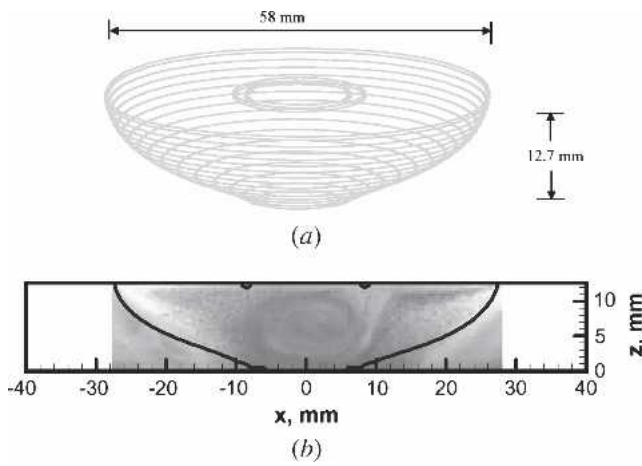


Fig. 14—(a) Computed iso-viscosity surface (5×10^6 kg/m-s) that defines viscoplastic flow region and TMAZ geometry. (b) Comparison of the numerically computed TMAZ geometry with the corresponding experimentally^[9] determined geometry. The welding velocity was 1.59 mm/s and the rotational speed was 637 rpm.

$$\dot{\epsilon} = \sqrt{\frac{2}{3} \left(\left(\frac{\partial u_1}{\partial x_1} \right)^2 + \left(\frac{\partial u_2}{\partial x_2} \right)^2 + \left(\frac{\partial u_3}{\partial x_3} \right)^2 + \frac{1}{2} \left(\frac{\partial u_1}{\partial x_2} + \frac{\partial u_2}{\partial x_1} \right)^2 + \frac{1}{2} \left(\frac{\partial u_1}{\partial x_3} + \frac{\partial u_3}{\partial x_1} \right)^2 + \frac{1}{2} \left(\frac{\partial u_2}{\partial x_3} + \frac{\partial u_3}{\partial x_2} \right)^2 \right)} \quad [A5]$$

IV. SUMMARY AND CONCLUSIONS

The equations of conservation of mass, momentum, and energy were numerically solved with appropriate boundary conditions to obtain 3D temperature and plastic flow fields during FSW. The heat generation rate was calculated from the tool geometry, rotational speed, and shear stress for yielding. The spatial variation of non-Newtonian viscosity was determined from the computed values of strain rate, temperature, and material properties. The following are the main findings. The computed results show that significant plastic flow occurs in close proximity of the tool. The plastic flow significantly affects heat transport within the work-piece, even for 6061 aluminum alloy that has a high thermal conductivity. The computed results show asymmetry of the temperature profiles around the tool because of the rotational and linear motion of the tool and asymmetry of heat generation around the tool pin surface. The cutoff viscosity above which no significant material flow occurs was found to be 5,000,000 Pa-s. The computed temperature *versus* time plots and the geometry of the TMAZ region agreed well with corresponding independent experimental results.

APPENDIX A

Calculation of strain rate

Recalling Eq. [5] from text, $\dot{\epsilon}$, the effective strain rate is given by:

$$\dot{\epsilon} = \left(\frac{2}{3} \epsilon_{ij} \epsilon_{ij} \right)^{1/2} \quad [A1]$$

where e_{ij} is the strain rate tensor, defined as:

$$\epsilon_{ij} = \frac{1}{2} \left(\frac{\partial u_i}{\partial x_j} + \frac{\partial u_j}{\partial x_i} \right) \quad [A2]$$

In expanded form the components of the strain tensor may be defined as:

$$\begin{aligned} \epsilon_{11} &= \frac{\partial u_1}{\partial x_1}; \quad \epsilon_{22} = \frac{\partial u_2}{\partial x_2}; \quad \epsilon_{33} = \frac{\partial u_3}{\partial x_3}; \\ \epsilon_{12} &= \frac{1}{2} \left(\frac{\partial u_1}{\partial x_2} + \frac{\partial u_2}{\partial x_1} \right); \quad \epsilon_{23} = \frac{1}{2} \left(\frac{\partial u_2}{\partial x_3} + \frac{\partial u_3}{\partial x_2} \right); \\ \epsilon_{31} &= \frac{1}{2} \left(\frac{\partial u_1}{\partial x_3} + \frac{\partial u_3}{\partial x_1} \right) \end{aligned} \quad [A3]$$

And the product of the stress tensor in expanded form may be expressed as:

$$\epsilon_{ij} \epsilon_{ij} = \epsilon_{11}^2 + \epsilon_{22}^2 + \epsilon_{33}^2 + 2(\epsilon_{12}^2 + \epsilon_{23}^2 + \epsilon_{31}^2) \quad [A4]$$

Finally, the strain rate in expanded form may be given as:

APPENDIX B

Numerical solution of the governing equations

Before discretizing the governing equations, the three equations of conservation of momentum and the energy conservation equation are rewritten in the following general form:

$$\frac{\partial}{\partial x_i} (\rho u_i \phi_j) = \frac{\partial}{\partial x_i} \left(\Gamma \frac{\partial \phi_j}{\partial x_i} \right) + S_j \quad [B1]$$

where ϕ = the general dependent variable, Γ = the diffusion coefficient, and S = the source term. The indices i or $j = 1, 2,$ and 3 represent the $x, y,$ and z directions respectively. Thus, the governing momentum equation as given by Eq. [2] may be modified into the general form:

$$\frac{\partial}{\partial x_i} (\rho u_i u_j) = \frac{\partial}{\partial x_i} \left(\Gamma \frac{\partial u_j}{\partial x_i} \right) + S_{u_j} \quad [B2]$$

where the source term for the momentum equations can be given as:

$$S_{u_j} = -\frac{\partial p}{\partial x_j} + \frac{\partial}{\partial x_i} \left(\mu \frac{\partial u_i}{\partial x_j} \right) - \rho U \frac{\partial u_j}{\partial x_j} \quad [B3]$$

Similarly, the energy equation given by Eq. [8] in the text may be rewritten as:

$$\rho C_p \frac{\partial (u_i T)}{\partial x_i} = \frac{\partial}{\partial x_i} \left(k \frac{\partial T}{\partial x_i} \right) + S_h \quad [B4]$$

where

$$S_h = \left[\{S(\theta)A_T/V\} - \rho C_p U \frac{\partial T}{\partial x_i} \right] \quad [\text{B5}]$$

The governing equations are discretized using a control volume method^[22] where the workpiece is divided into small rectangular control volumes. Each control volume surrounds a grid point where the scalar variables are stored. Vectors such as the velocities are stored at grid points that are staggered with respect to those of scalar variables such as pressure and temperature to ensure the stability of numerical calculation. Thus, the control volumes for scalars are different from those for the vectors. The discretized equations are formulated by integrating the corresponding governing equation over the control volumes using fully implicit hybrid power law scheme. The final discretized form of Eq. [B1] takes the following form:^[22]

$$a_P \phi_P = \sum_{nb} (a_{nb} \phi_{nb}) + S_U \Delta V \quad [\text{B6}]$$

where ϕ = a general variable such as velocity or enthalpy, a = the coefficient of the variables calculated based on the power law scheme, subscript nb = the neighbors of a grid point P , and ΔV is the volume of the control volume. The coefficient of ϕ at the point P is defined in terms of neighboring grid points as follows:

$$a_P = \sum_{nb} a_{nb} - S_P \Delta V \quad [\text{B7}]$$

The terms S_U and S_P are the coefficients of the linearized source term, defined as:

$$S = S_U + S_P \phi \quad [\text{B8}]$$

Among the velocity boundary conditions, the velocities are known on the shoulder surface. However, implementation of known fixed velocity boundary conditions (U_F) at the tool pin surface needs some discussion. Eq. [B6] can be modified by assigning a large negative value to S_P and S_P times U_F to S_U such that the first term on the right-hand side becomes negligible, yielding $\phi_P = U_F$.

The implementation of heat flux at the top shoulder/workpiece interface also needs some discussion. Recalling Eq. [11] from text:

$$\left(k \frac{dT}{dz} \right) \Big|_{z=z_{\max}} = q_1(x, y) \quad [\text{B9}]$$

Integrating this equation over the topmost boundary control volume, the temperatures at the topmost z grids, nk , may be related to the temperature at the grid points at $nk - 1$ as:

$$T_{i,j,nk} = T_{i,j,nk-1} + \frac{q_1(x, y)}{k_{i,j,nk}} \Delta z \quad [\text{B10}]$$

where $k_{i,j,nk}$ = the space-dependent thermal conductivity values at the topmost z grids. Finally, the equations at $(nk - 1)$ grid points can be obtained by combining Eqs. [B6] and [B10] as follows:

$$S_U = S_U + a_T \left[\frac{q_1(x, y)}{k_{i,j,nk}} \Delta z \right] / \Delta V \quad [\text{B11}]$$

$$S_P = S_P + (a_T / \Delta V) \quad [\text{B12}]$$

The temperature boundary condition at the bottom surface can be implemented as follows. Recalling Eq. [14] from text,

$$\left(k \frac{dT}{dz} \right) \Big|_{z=0} = h_b(T - T_a) \quad [\text{B13}]$$

Integrating the equation over bottom control volume ($k = 1$), the enthalpy may be expressed in terms of the grid point values at $k = 2$

$$T_{i,j,1} = \frac{(k_1/\Delta z)T_{i,j,2} + h_b h_a}{\left(\frac{k_1}{\Delta z} + h_b \right)} = C_1 T_{i,j,2} + C_2 \quad [\text{B14}]$$

where

$$C_1 = \frac{(k_1/\Delta z)}{[(k_1/\Delta z) + h_b]} \quad \text{and} \quad C_2 = \frac{h_b h_a}{[(k_1/\Delta z) + h_b]}$$

Finally, the equations at grid points for $k = 2$ may be obtained by combining Eqs. [B6] and [B14], and Eq. [6] may be represented in terms of modified S_U and S_P as:

$$S_U = S_U + C_2 / \Delta V \quad [\text{B15}]$$

$$S_P = S_P + (C_1 a_B / \Delta V) \quad [\text{B16}]$$

Accurate calculation of temperature and velocity fields requires the use of a very fine grid system. A typical grid system used in the current study contained $132 \times 130 \times 17$ grid points, and the corresponding computational domain had dimensions of 37.0 mm in length, 24.0 mm in width, and 12.7 mm in depth. Spatially nonuniform grids with finer grid spacing near the heat source were used for maximum resolution of variables.

Two criteria were used to test for convergen magnitude of residuals of enthalpy and three velocities, and the overall heat balance. The residual for any variable ϕ is defined as:

$$R = \frac{\sum_{\text{domain}} \left| \frac{\sum_{nb} (a_{nb} \phi_{nb}) + S_U \Delta V}{a_P} - \phi_P \right|}{\sum_{\text{domain}} |\phi_P|} \quad [\text{B17}]$$

Values of R less than 5.0×10^{-5} were accepted as converged solution. Heat balance ratio is given by:

$$\theta = \left| \frac{\text{net heat input}}{\text{total heat out} + \text{heat accumulation}} \right| \quad [\text{B18}]$$

The heat balance ratio θ within $0.99 \leq \theta \leq 1.01$ was accepted as converged solution. Several stricter convergence criteria did not change the final results. A single

run typically took about 3000 iterations to converge, which took about 15 minutes in a dedicated PC with 3.06 GHz Intel P4 CPU and 512 MB PC2700 DDR-SDRAM.

REFERENCES

1. W.M. Thomas, E.D. Nicholas, J.C. Needham, M.G. Murch, P. Templesmith, and C.J. Dawes: International patent application no. PCT/GB92/02203 and GB patent application no. 9125978.9, 1991.
2. M.J. Russel and H.R. Shercliff: *Proceedings of the 7th International Conference on "Joints in Aluminum" (INALCO '98)*, The Welding Institute, Cambridge, U.K., 1998, vol. 2, pp. 185-95.
3. J.E. Gould and Z. Feng: *J. Mater. Process. Manuf. Sci.*, 1998, vol. 7, pp. 185-94.
4. H. Schmidt, J. Hattel, and J. Wert: *Modeling Simulations Mater. Sci. Eng.*, 2004, vol. 12, pp. 143-57.
5. Ø. Frigaard, Ø. Grong, and O.T. Midling: *Metall. Mater. Trans. A*, 2001, vol. 32, pp. 1189-200.
6. Y.J. Chao, X. Qi, and W. Tang: *Trans. ASME*, 2003, vol. 125, pp. 138-45.
7. M. Song and R. Kovacevic: *Proc. Instn. Mech. Engrs. Part B: J. Eng. Manuf.*, 2003, vol. 217 (B1), pp. 73-85.
8. M. Song and R. Kovacevic: *Int. J. Machine Tool Manuf.*, 2003, vol. 43 (6), pp. 605-15.
9. M. Song and R. Kovacevic: *Proc. Instn. Mech. Engrs. Part B: J. Eng. Manuf.*, 2004, vol. 218, pp. 17-33.
10. M.Z.H. Khandkar, J.A. Khan, and A.P. Reynolds: *Sci. Technol. Weld. Joining*, 2003, vol. 8 (3), pp. 165-74.
11. P.A. Colegrove and H.R. Shercliff: *Sci. Technol. Weld. Joining*, 2004, vol. 9 (4), pp. 345-51.
12. T.U. Seidel and A.P. Reynolds: *Sci. Technol. Weld. Joining*, 2003, vol. 8, pp. 175-83.
13. C.B. Smith, G.B. Bendzsak, T.H. North, J.F. Hinrichs, J.S. Noruk, and R.J. Heideman: *Proceedings of the 9th International Conference on Computer Technology in Welding*, Detroit, 2000, pp. 475-86.
14. P. Ulysse: *Int. J. Machine Tools Manuf.*, 2002, vol. 42, pp. 1549-57.
15. P.A. Colegrove and H.R. Shercliff: *J. Mater. Process. Technol.*, 2005, in press.
16. W. Zhang, G.G. Roy, J.W. Elmer, and T. DebRoy: *J. Appl. Phys.*, 2003, vol. 93, pp. 3022-33.
17. T. Sheppard and D.S. Wright: *Metal. Technol.*, 1979, vol. 6, pp. 215-23.
18. O.C. Zienkiewicz and I.C. Cormeau: *Int. J. Numer. Methods Eng.*, 1974, vol. 8, pp. 821-45.
19. T. Sheppard and A. Jackson: *Mater. Sci. Technol.*, 1997, vol. 13, pp. 203-09.
20. *ASM Handbook*, vol. 2, ASM International, Columbus, OH, 1990, pp. 102-03.
21. D.R. Lesuer, G.J. Kay, and M.M. LeBlanc: "Modeling Large-Strain, High-Rate Deformation in Metals," Third Biennial Tri-Laboratory Engineering Conference on Modeling and Simulation, Pleasanton, CA, November 3-5, 1999. Also available on the web at <http://www.llnl.gov/tid/lof/documents/pdf/243782.pdf> as a report of the Lawrence Livermore National Laboratory Report #UCRL-JC-134118 dated July 20, 2001.
22. S.V. Patankar: *Numerical Heat Transfer and Fluid Flow*, Hemisphere Publishing Corporation, New York, NY, 1980.
23. X. He, J. Elmer, and T. DebRoy: *J. Appl. Phys.*, 2005, vol. 97, p. 84909.
24. A. De and T. DebRoy: *Welding J.*, 2005, vol. 84 (7), pp. 101-12.
25. S. Mishra and T. DebRoy: *J. Phys. D*, 2005, vol. 38, pp. 2977-85.
26. W. Zhang, T. DebRoy, and J.W. Elmer: *Sci. Technol. Weld. Joining*, 2005, vol. 10 (5), pp. 574-82.
27. W. Zhang, T. DebRoy, T.A. Palmer, and J.W. Elmer: *Acta Mater.*, 2005, vol. 53 (16), pp. 4441-53.
28. S. Mishra and T. DebRoy: *J. Appl. Phys.*, 2005, vol. 98, p. 044902.
29. P.J. Halley and M.E. Mackay: *J. Rheol.*, 1994, vol. 38 (1), pp. 41-51.